WHEN PROMPT MEETS FREQUENCY LEARNING FOR EFFICIENT IMAGE RESTORATION

Anonymous authors
Paper under double-blind review

ABSTRACT

Image restoration, as a longstanding task, aims to recover the missing details and remove degradations from a corrupted observation. Inspired by the success of prompt learning in natural language processing, many prompt-based approaches have been developed for various image restoration tasks. However, these algorithms mostly operate in the spatial domain. As frequency learning plays an important role in image restoration by reducing the spectra discrepancy between degraded/sharp image pairs, this study explores the potential of frequency prompts for efficient image restoration by proposing a plug-and-play mechanism, which mainly comprises a prompt generation module and a prompt integration module. Specifically, the former encodes different frequency information by aggregating the pre-defined learnable parameters under the guidance of implicitly decomposed spectra of input features. Subsequently, to dynamically guide reconstruction, the learned prompts are embedded into the spectra of features via dual-dimensional attention for effective frequency learning. To demonstrate the effectiveness of our mechanism, we conduct experiments on general and all-in-one image restoration tasks. By incorporating it into a CNN-based backbone, the model achieves state-of-the-art performance on **15** benchmark datasets for five representative image restoration tasks. Furthermore, equipped with our mechanism, a pure Transformer network performs favorably against state-of-the-art algorithms under two all-in-one settings.

1 INTRODUCTION

Due to the physical limitations of low-end sensors or terrible weather, various degradations (haze, noise, and blur) are often involved in acquired images (Su et al., 2022), which will degrade the visibility and impact the performance of models for downstream tasks. As an ill-posed problem, image restoration aims to remove those undesired degradations from observations and recover the missing details. Early approaches attempted to deal with its ill-posedness by proposing various assumptions and hand-crafted priors to reduce the solution space (Song et al., 2022; Zhang et al., 2022). In recent years, the rapid development of deep learning has spawned a great number of frameworks built on convolutional neural networks (CNNs), which can learn more robust priors from large-scale data. By means of varied advanced modules, including residual connections (Liu et al., 2019; Ruan et al., 2022), U-shaped architectures (Mao et al., 2021; Cho et al., 2021), and attention mechanisms (Qin et al., 2020; Cui et al., 2023d; Zhang et al., 2018b), these methods have achieved promising performance on multifarious image restoration tasks.

Subsequently, many general image restoration methods have been developed, which can perform well on a range of tasks after separate training (Chen et al., 2022; 2021a; Cui et al., 2023a). For example, MPRNet (Zamir et al., 2021) adopts a multi-stage CNN-based architecture to break down the recovery process into several manageable steps. Transformers have also been introduced into this track by performing self-attention within different scopes (Tsai et al., 2022; Liang et al., 2021; Wang et al., 2022; Li et al., 2023a) and dimensions (Zamir et al., 2022a). However, these solutions need individual training processes and copies when applied to different tasks, which is not practical for resource-constrained scenarios. To alleviate these issues, the recent all-in-one topic has garnered significant attention by training a unified model for a series of degradations (Lin et al., 2024; Zhang et al., 2023; Yang et al., 2023). For instance, AirNet (Li et al., 2022) is one of the pioneering methods to recover clean images in an all-in-one fashion. It works by contrastively learning the degradation representations, which are then used to restore the sharp image.

More recently, prompt learning originating from natural language processing (Zhou et al., 2022a;b) has been incorporated into general and all-in-one image restoration and has advanced performance by providing adaptive learning ability. These prompt-based methods encode the degradation priors using the produced or pre-set prompts (Potlapalli et al., 2024; Yu et al., 2024; Li et al., 2023b; Luo et al., 2021; Gao et al., 2023; Ai et al., 2023), which are then used to guide the restoration process. For example, PromptIR (Potlapalli et al., 2024) addresses all-in-one image restoration using the input-conditioned prompts that learn the knowledge of different degradation types. SelfPromer (Wang et al., 2024a) formulates the prompts based on depth cues, requiring an expensive depth estimator for supervision. However, these prompt-based methods mostly operate in the spatial domain without investigating the significance of frequency learning in prompts, which is also beneficial for high-fidelity image restoration.

In this paper, we present a plug-and-play prompt-based mechanism by formulating prompts from the perspective of frequency. To this end, we first embed crucial information about different subbands into learnable parameters with the guidance of different frequencies produced via a simple **frequency decomposition** method. Then, the learned prompts interact with the input features in the **frequency domain** via **dual-dimensional** attention weights. Overall, the resources for learning prompts and the aggregation method of injecting prompts into features are both from the frequency perspectives, resulting in consistency and effective frequency learning. Moreover, the dual-dimensional attention weights facilitate the full use of frequency signals encoded in prompts. By doing these, our mechanism enables the model to effectively recover clean images by dynamically refining frequency signals.

Our simple yet effective plug-and-play frequency prompt mechanism can be easily applied to CNN-based and Transformer-based architectures. Specifically, combined with a CNN-based backbone, our mechanism helps the model achieve state-of-the-art performance on **15** datasets for a range of representative image restoration tasks, including image dehazing, desnowing, deraining, defocus deblurring, and low-light image enhancement. Equipped with our mechanism, a pure Transformer model performs favorably against state-of-the-art algorithms under two all-in-one settings.

2 Related Work

2.1 Image Restoration

Given a corrupted image, image restoration aims to recover a clean image by removing degradations and reconstructing missing details. The development of deep learning has spawned a great number of methods, which can be roughly divided into three classes in terms of task: task-specific (Qin et al., 2020; Liu et al., 2019; Cho et al., 2021; Ruan et al., 2022), task-agnostic (or general) (Liang et al., 2021; Wang et al., 2022; Zamir et al., 2022a; Cui et al., 2023a;c), and all-in-one (Yang et al., 2023; Potlapalli et al., 2024; Yu et al., 2024; Li et al., 2023b; Luo et al., 2021). The task-specific methods can only perform well on a specific task, while task-agnostic ones can be applied to several tasks but need separate training on each dataset. These two categories have made great progress in terms of performance, which can be attributed to advanced designs for CNN- and Transformer-based frameworks. The all-in-one task has recently been a hot topic in image restoration because the all-in-one models can deal with multiple degradation types by training a single model once, which is suitable for resource-constrained scenarios. In this paper, we conduct experiments on both general and all-in-one image restoration tasks to demonstrate the effectiveness of the proposed method.

2.2 Prompt Learning

Prompt learning is originally used in natural language processing to finetune a trained model to a downstream task by providing in-context and task-specific information. Inspired by this, this technique has been adopted in image restoration algorithms to encode degradation information (Yu et al., 2024; Li et al., 2023b; Wang et al., 2024b; Zhou et al., 2024). PromptRestorer (Wang et al., 2023) uses raw degradation features to generate prompts for general tasks and incorporates prompts from global and local perspectives via self-attention units. PromptCIR (Li et al., 2024) applies spatial prompts (Potlapalli et al., 2024) for blind compressed image restoration. SelfPromer (Wang et al., 2024a) formulates the prompt by considering the estimated depth cues for image dehazing. In the context of the all-in-one setting, PromptIR (Potlapalli et al., 2024) introduces a drop-in prompt block to dynamically adjust representations for high-fidelity image restoration. Subsequently, DA-

CLIP (Luo et al., 2021) utilizes content embedding yielded by a large vision-language model to aggregate prompts for universal image restoration. Nevertheless, these prompt-based approaches primarily leverage prompts in the spatial domain without exploring the utility in the frequency domain. In this study, to explore the potential of frequency prompts for image restoration, we use different frequencies generated via an extremely **lightweight** frequency decomposition strategy to encode frequency information into prompts, and then inject prompts into the input features in the **frequency** domain via **dual-dimensional** attention, ensuring the domain consistency between the source of producing prompts and injecting method. Furthermore, our dual-dimensional operation facilitates full use of the acquired knowledge in prompts.

3 Frequency Prompt Mechanism (FPM)

Prompt learning is derived from natural language processing to achieve parameter-efficient fine-tuning of pre-trained large models to a target task. In this study, we explore the potential of this technique in the spectral domain to encode the different frequency signals for adaptive and high-fidelity image restoration. The design principle of our frequency prompt mechanism (FPM) is to generate the prompts from the frequency perspective and incorporate them into the spectra of input features for effective frequency learning. To achieve these goals, we present a prompt generation module (PGM) and a prompt integration module (PIM). Finally, FPM is realized by successively using these two modules, which can be formally expressed as:

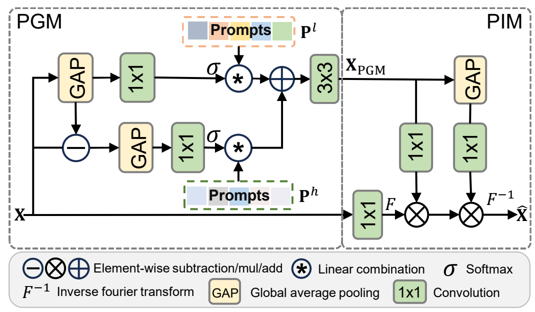

Figure 1: Illustration of our frequency prompt mechanism, containing a prompt generation module (PGM) and a prompt integration module (PIM).

$$\hat{\mathbf{X}} = \mathrm{PIM}\left(\mathrm{PGM}(\mathbf{X}, \mathbf{P}^l, \mathbf{P}^h), \mathbf{X}\right) \tag{1}$$

where $\mathbf{X}$ and $\hat{\mathbf{X}} \in \mathbb{R}^{C\times H\times W}$ denote the input features and output of FPM, respectively. C, H, and W are the channel, height, and width of features. $\mathbf{P}^l$ and $\mathbf{P}^h \in \mathbb{R}^{B\times C\times \hat{H}\times \hat{W}}$ are prompts encoding the low- and high-frequency information. B specifies the number of prompts and $\hat{H}\times\hat{W}$ is resolution.

3.1 Prompt Generation Module (PGM)

The PGM is responsible for encoding the informative information of different frequency subbands into prompts. To this end, we first leverage a lightweight frequency decouple method and then use the corresponding frequencies to aggregate the preset learnable parameters.

To be specific, as illustrated in Figure 1, assuming $\mathbf{X}$ is the input, a global average pooling (GAP) layer is applied to yield the low-frequency signals, where GAP serves as a kind of low-pass filter by computing the average value of the feature. Accordingly, the high-frequency component can be easily produced by removing this resulting low-frequency subband from the input $\mathbf{X}$. Subsequently, the attention weights for aggregating the prompts are produced by 1×1 convolution layers and softmax functions. After adding the prompts that are expected to encode the frequency information, the output of PGM is obtained via a 3×3 convolution. Overall, the process of PGM is formally summarized as:

$$\mathbf{X}_{\mathrm{PGM}} = \mathrm{Conv}_{3\times 3}\left(\sum_{b=1}^{B} W_b^l \mathbf{P}_b^l + \sum_{b=1}^{B} W_b^h \mathbf{P}_b^h\right), \tag{2}$$

$$W^l = \mathrm{Softmax}\left(\mathrm{Conv}_{1\times 1}^{l}\left(\mathrm{GAP}(\mathbf{X})\right)\right), \quad W^h = \mathrm{Softmax}\left(\mathrm{Conv}_{1\times 1}^{h}\left(\mathbf{X} - \mathrm{GAP}(\mathbf{X})\right)\right) \tag{3}$$

where $\mathbf{X}_{\mathrm{PGM}} \in \mathbb{R}^{C\times\hat{H}\times\hat{W}}$ is the output of PGM. GAP and Softmax are global average pooling and Softmax operators, respectively. $\mathrm{Conv}_{1\times 1}$ denotes a 1×1 convolution with the reduction rate of $\frac{C}{B}$ and $\mathrm{Conv}_{3\times 3}$ is a 3×3 convolution layer for final refinement. Before being input into PIM, $\mathbf{X}_{\mathrm{PGM}}$ is spatially interpolated to align with the original input for further integration.

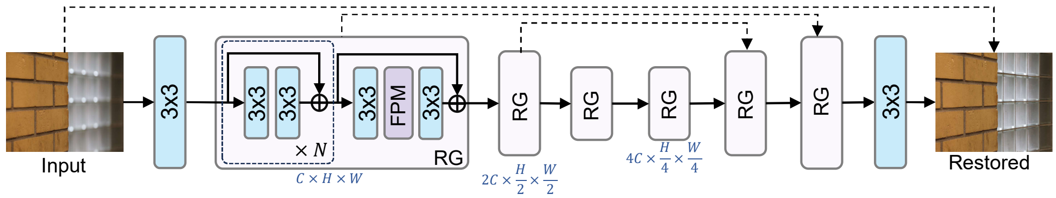

Figure 2: The CNN-based model for general image restoration. FPM is employed in a residual block.

3.2 Prompt Integration Module (PIM)

The PIM is designed to integrate the combined frequency prompts into the original input features. Different from existing prompt-based schemes (Potlapalli et al., 2024; Wang et al., 2023; Zhou et al., 2024) that use cross-attention modules, we instead adopt a more natural solution, refining the spectra of features.

Specifically, based on the output of PGM, $\mathbf{X}_{\mathrm{PGM}}$, PIM first uses a couple of convolution layers and GAP to generate spatial and channel attention weights, which are then utilized to modulate the Fourier spectra of the input features. This process can be formally expressed by:

$$\hat{\mathbf{X}} = F^{-1}\left(W_c W_s \left(F\left(\mathrm{Conv}_{1\times1}(\mathbf{X})\right)\right)\right), \tag{4}$$

$$W_s = \mathrm{Conv}^{\mathrm{s}}_{1\times1}(\mathbf{X}_{\mathrm{PGM}}), \quad W_c = \mathrm{Conv}^{c}_{1\times1}(\mathrm{GAP}(\mathbf{X}_{\mathrm{PGM}})) \tag{5}$$

where F and F^{-1} denote the fast Fourier transform and the inverse operator, respectively. $W_c \in \mathbb{R}^{C\times1\times1}$ and $W_s \in \mathbb{R}^{C\times H\times W}$ are the generated channel and spatial attention weights.

4 Experiments

In this section, we conduct comprehensive experiments in two cases, *i.e.,* general and all-in-one image restoration tasks, to demonstrate the effectiveness of our proposed mechanism. In each case, we first delineate the adopted backbone and deployment method of our FPM. Next, we introduce the implementation details and used datasets. Finally, the experimental results are presented.

4.1 General Image Restoration

To purely verify the efficacy of our design, we integrate our design with a classic U-shaped CNN-based backbone. As illustrated in Figure 2, the model consists of three scales. Each residual group (RG) contains $N+1$ residual blocks, and the last one accommodates our FPM between two convolutions.

The degraded input image is processed by a 3×3 convolution layer to generate embedding features. After going through the three-scale encoder and decoder networks, the restored image is produced by another 3×3 convolution layer and image-level residual connection.

4.1.1 Implementation Details

For general image restoration, we conduct experiments by separately training models on different datasets for five representative image restoration tasks. Specifically, for dehazing, we evaluate our methods on synthetic daytime datasets (SOTS-Indoor (Li et al., 2018), SOTS-Outdoor (Li et al., 2018), Haze4K (Liu et al., 2021)), nighttime datasets (GTA5 (Yan et al., 2020), NHR (Zhang et al., 2020)), remote sensing datasets (SateHaze1k (Huang et al., 2020)-Thin, Moderate, Thick), and a real-world dataset (DenseHaze (Ancuti et al., 2019)). Moreover, the models are tested on the widely used CSD (Chen et al., 2021b), SRRS (Chen et al., 2020), and Snow100K (Liu et al., 2018) for image desnowing, DPDD (Abuolaim & Brown, 2020) for defocus deblurring, LOL-v2-Synthetic (Yang et al., 2021) for low-light image enhancement, and Test2800 (Fu et al., 2017) for deraining.

The model is trained using the Adam (Kingma & Ba, 2014) optimizer and dual-domain L_1 loss functions (Cho et al., 2021; Cui et al., 2023a). Random horizontal flips are used for data augmentation. Following previous methods (Cui et al., 2023a; Zamir et al., 2021), we use different numbers of

Table 1: Image dehazing comparisons on the synthetic daytime datasets (SOTS-Indoor (Li et al., 2018), SOTS-Outdoor (Li et al., 2018)) and a real-world dataset (Dense-Haze (Ancuti et al., 2019)).

Method	SOTS-Indoor		SOTS-Outdoor		Dense-Haze		Average	
	PSNR	SSIM	PSNR	SSIM	PSNR	SSIM	PSNR	SSIM
MSBDN (Dong et al., 2020a)	33.67	0.985	33.48	0.982	15.37	0.49	27.51	0.819
FFA-Net (Qin et al., 2020)	36.39	0.989	33.57	0.984	14.39	0.45	28.12	0.808
AECR-Net (Wu et al., 2021)	37.17	0.990	-	-	15.80	0.47	-	-
DeHamer (Guo et al., 2022)	36.63	0.988	35.18	0.986	16.62	0.56	29.48	0.845
PMNet (Ye et al., 2022)	38.41	0.990	34.74	0.985	16.79	0.51	29.98	0.828
MAXIM (Tu et al., 2022)	38.11	0.991	34.19	0.985	-	-	-	-
FocalNet (Cui et al., 2023a)	40.82	0.996	37.71	0.995	17.07	0.63	31.87	0.874
DEA-Net (Chen et al., 2024)	40.20	0.993	36.03	0.989	-	-	-	-
FSNet-S (Cui et al., 2023b)	40.47	0.996	37.24	0.994	17.00	0.65	31.57	0.880
MB-TaylorFormer-B (Qiu et al., 2023)	40.71	0.992	37.42	0.989	16.66	0.56	31.60	0.847
Ours	**40.86**	**0.996**	**37.86**	**0.995**	**17.33**	**0.65**	**32.02**	**0.880**

Table 2: Image dehazing comparisons on the remote sensing SateHaze1k (Huang et al., 2020) dataset. The models are separately trained and tested on each subset.

Methods	Thin		Moderate		Thick		Average	
	PSNR	SSIM	PSNR	SSIM	PSNR	SSIM	PSNR	SSIM
AOD-Net (Li et al., 2017)	19.54	0.854	20.10	0.885	15.92	0.731	18.52	0.823
H2RL-Net (Chen et al., 2021c)	20.91	0.880	22.34	0.906	17.41	0.768	20.22	0.851
FCFT-Net (Li & Chen, 2020)	23.59	0.913	22.88	0.927	20.03	0.816	22.17	0.885
Uformer (Wang et al., 2022)	22.82	0.907	24.47	0.939	20.36	0.815	22.55	0.887
C^2PNet (Zheng et al., 2023)	19.62	0.880	24.79	0.940	16.83	0.790	20.41	0.870
Restormer (Zamir et al., 2022a)	23.08	0.912	24.73	0.933	18.58	0.762	22.13	0.869
Trinity-Net (Chi et al., 2023)	21.55	0.884	23.35	0.895	20.97	0.823	21.96	0.867
FocalNet (Cui et al., 2023a)	24.16	0.916	25.99	0.947	21.69	0.847	23.95	0.903
Ours	**24.27**	**0.976**	**26.42**	**0.978**	**22.81**	**0.955**	**24.50**	**0.970**

Table 3: Image dehazing comparisons on the Haze4K (Liu et al., 2021) dataset.

Method	DehazeNet	AOD-Net	GDN	MSBDN	FFA-Net	PMNet	FSNet	**Ours**
PSNR	19.12	17.15	23.29	22.99	26.96	33.49	34.12	**34.14**
SSIM	0.84	0.83	0.93	0.85	0.95	0.98	0.99	**0.99**

Table 4: Image dehazing comparisons on the nighttime NHR (Zhang et al., 2020) dataset.

Method	GS	MRPF	MRP	OSFD	HCD	FSNet-S	FocalNet	**Ours**
PSNR	17.32	16.95	19.93	21.32	23.43	24.35	25.35	**26.24**
SSIM	0.629	0.667	0.777	0.804	0.953	0.965	0.969	**0.972**

Table 5: Image dehazing comparisons on the nighttime GTA5 (Yan et al., 2020) dataset.

Method	GS	MRP	Ancuti *et al.*	Yan *et al.*	CycleGAN	Jin *et al.*	FocalNet	**Ours**
PSNR	21.02	20.92	20.59	27.00	21.75	30.38	30.65	**30.73**
SSIM	0.639	0.646	0.623	0.850	0.696	0.904	0.909	**0.911**

residual blocks in each RG according to the complexity of tasks. The number of prompts B is set to 5. All experiments are performed on an NVIDIA Tesla A100 GPU. More details of the used datasets and specific training configurations are provided in the Appendix.

Table 6: Image desnowing comparisons on CSD (Chen et al., 2021b), SRRS (Chen et al., 2020), and Snow100K (Liu et al., 2018).

	CSD		SRRS		Snow100K		Average	
Method	PSNR	SSIM	PSNR	SSIM	PSNR	SSIM	PSNR	SSIM
DesnowNet (Liu et al., 2018)	20.13	0.81	20.38	0.84	30.50	0.94	23.67	0.86
All in One (Li et al., 2020)	26.31	0.87	24.98	0.88	26.07	0.88	25.79	0.88
JSTASR (Chen et al., 2020)	27.96	0.88	25.82	0.89	23.12	0.86	25.63	0.88
HDCW-Net (Chen et al., 2021b)	29.06	0.91	27.78	0.92	31.54	0.95	29.46	0.93
MSP-Former (Chen et al., 2023)	33.75	0.96	30.76	0.95	33.43	**0.96**	32.65	0.96
TransWeather (Valanarasu et al., 2022)	31.76	0.93	28.29	0.92	31.82	0.93	30.62	0.93
FSNet-S (Cui et al., 2023b)	35.33	0.98	31.39	0.98	33.36	0.95	33.36	0.97
FocalNet (Cui et al., 2023a)	37.18	0.99	31.34	0.98	33.53	0.95	34.02	0.97
Ours	**37.31**	**0.99**	**31.78**	**0.98**	**33.61**	0.95	**34.23**	**0.97**

Table 7: Image defocus deblurring comparisons on the DPDD (Abuolaim & Brown, 2020) dataset.

	Indoor Scenes				Outdoor Scenes				Combined			
Method	PSNR↑	SSIM↑	MAE↓	LPIPS↓	PSNR	SSIM	MAE	LPIPS	PSNR	SSIM	MAE	LPIPS
EBDB (Karaali & Jung, 2017)	25.77	0.772	0.040	0.297	21.25	0.599	0.058	0.373	23.45	0.683	0.049	0.336
DMENet (Lee et al., 2019)	25.50	0.788	0.038	0.298	21.43	0.644	0.063	0.397	23.41	0.714	0.051	0.349
JNB (Shi et al., 2015)	26.73	0.828	0.031	0.273	21.10	0.608	0.064	0.355	23.84	0.715	0.048	0.315
DPDNet (Abuolaim & Brown, 2020)	26.54	0.816	0.031	0.239	22.25	0.682	0.056	0.313	24.34	0.747	0.044	0.277
KPAC (Son et al., 2021)	27.97	0.852	0.026	0.182	22.62	0.701	0.053	0.269	25.22	0.774	0.040	0.227
IFAN (Lee et al., 2021)	28.11	0.861	0.026	0.179	22.76	0.720	0.052	0.254	25.37	0.789	0.039	0.217
DRBNet (Ruan et al., 2022)		-				-			25.73	0.791	-	0.183
Restormer (Zamir et al., 2022a)	28.87	0.882	0.025	0.145	23.24	0.743	0.050	0.209	25.98	0.811	0.038	0.178
FocalNet (Cui et al., 2023a)	29.10	0.876	0.024	0.173	23.41	0.743	0.049	0.246	26.18	0.808	0.037	0.210
Lin *et al* (Lin et al., 2024)	29.11	**0.889**	-	-	23.35	0.748	-	-	26.15	**0.817**	-	-
FSNet (Cui et al., 2023b)	29.14	0.878	0.024	0.166	23.45	0.747	0.050	0.246	26.22	0.811	0.037	0.207
Ours	**29.38**	0.883	**0.023**	**0.145**	**23.49**	**0.753**	**0.049**	**0.208**	**26.35**	0.816	**0.036**	**0.178**

Table 8: Low-light image enhancement results on the LOL-v2 (Yang et al., 2021) dataset.

Method	EnGAN	RUAS	FIDE	DRBN	KinD	Restormer	MIRNet	SNR-Net	Retinexformer	Ours
PSNR	16.57	16.55	15.20	23.22	13.29	21.41	21.94	24.14	25.67	**26.21**
SSIM	0.734	0.652	0.612	0.927	0.578	0.830	0.876	0.928	0.930	**0.958**

Table 9: Image deraining comparisons on the Test2800 (Fu et al., 2017) dataset.

Method	DerainNet	UMRL	RESCAN	PreNet	MSPFN	MPRNet	FSNet	**Our**
PSNR	24.31	29.97	31.29	31.75	32.82	33.64	33.64	**33.72**
SSIM	0.861	0.905	0.904	0.916	0.930	0.938	0.936	**0.937**

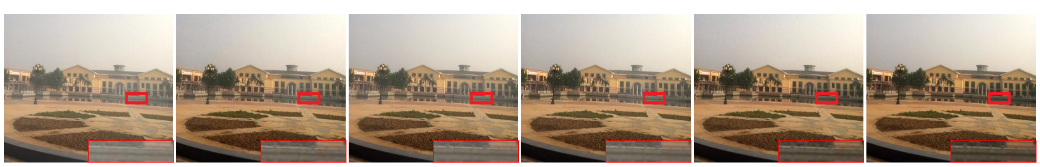

19.18 dB	27.23 dB	24.82 dB	27.18 dB	32.90 dB	∞
Hazy Image	FFA-Net	MAXIM	DeHamer	Ours	GT

Figure 3: Image dehazing comparisons on the SOTS-Outdoor (Li et al., 2018) dataset.

4.1.2 Experimental Results

The quantitative results for image dehazing, desnowing, defocus deblurring, low-light image enhancement, and deraining are presented in Table 1-5, Table 6, Table 7, Table 8, and Table 9, respectively. The best scores in the tables are highlighted in **bold**. From the tables, we can see that our network achieves the best performance on most metrics. It is worth mentioning that our results are obtained

Table 10: Break-down ablations.

Method	Baseline	PGM	PIM	Full
PSNR	31.33	33.82	34.54	35.18
GFLOPs	15.44	19.06	16.26	19.89

Table 11: Different alternatives to PIM.

Method	Spatial Domain	Cross Attention	PIM w/o Channel	Ours
PSNR	34.25	34.17	34.85	**35.18**

Table 12: Frequencies used to aggregate prompts in PGM.

Net	Frequency	PSNR
(a)	Baseline	31.33
(b)	Low	33.24
(c)	High	31.47
(d)	None	32.34
(e)	Low/Low	33.72
(f)	High/High	33.16
(g)	Ours	**33.82**

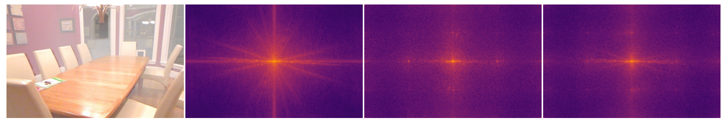

Hazy Image F(GT-Input) F(GT-Low) F(GT-High)

Figure 4: The spectra of differences between ground truth and hazy image, low-frequency prompt and high-frequency prompt results. The latter two images are produced using only the low-frequency and high-frequency prompts, respectively, during the inference of our dehazing model. F is the fast Fourier transform. Our frequency prompts can recover the corresponding frequency signals.

by merging our proposed mechanism into a simple CNN-based backbone. Figure 3 shows that our model generates a more favorable image than competitors by removing more haze degradations. These results demonstrate that our novel design is beneficial for high-fidelity image restoration. Due to the space limit, the qualitative comparisons for more tasks are presented in the Appendix.

4.1.3 Ablation Studies

We perform the ablation results by training a dehazing model ($N = 0$) on RESIDE-Indoor (Li et al., 2018) for 300 epochs and testing on SOTS-Indoor (Li et al., 2018). More ablation studies can be found in the Appendix.

Effects of individual components. The baseline model is obtained by removing our FPM from the dehazing model. Table 10 shows that the baseline model achieves 31.33 dB PSNR on the SOTS-Indoor (Li et al., 2018) dataset. Next, equipped with PGM, the model achieves a gain of 2.49 dB PSNR by directly adding the output of PGM to input features in the spatial domain. The PIM version, taking the original input features as input and imposing the attention weights on input features in the spectral domain, outperforms the baseline by 3.21 dB PSNR. Taken together, the full model obtains the best performance, suggesting the effectiveness of frequency-inspired prompt design.

Design choices for integration method in PIM. We further explore the influence of the integration method in PIM by performing experiments with several alternatives. Table 11 shows that applying the attention weights produced by PIM to input features in the spatial domain results in a degradation of 0.93 dB PSNR compared to our frequency version. The widely adopted cross-attention method in existing prompt-based algorithms only achieves 34.17 dB PSNR. Using only the spatial attention in PIM is superior to our bi-dimensional variant. The results reveal that, besides the generation of prompts, the integration method also plays a significant role in exploring the potential of prompts.

Design choices for PGM. To verify the efficacy of our PGM design, we experiment using different combinations of frequencies to aggregate prompts. Table 12 shows that the model using the low-frequency or high-frequency prompts both outperforms the baseline model, demonstrating the effectiveness of prompt learning for image restoration. The input-conditioned prompts (Table 12 e,f) are superior to the counterpart, *None* (Table 12 d), where the preset learnable parameters are directly injected into the input features without the guidance of frequency-based attention weights. Our design, employing different frequencies for guidance, attains the best performance.

Visual results of our mechanism. To understand the mechanisms of our frequency prompt design more intuitively, we compute the Fourier spectra of differences between ground truth and the input image, low-frequency and high-frequency prompt results. For example, the low-frequency result is obtained by removing the high-frequency prompts during the inference of our dehazing model.

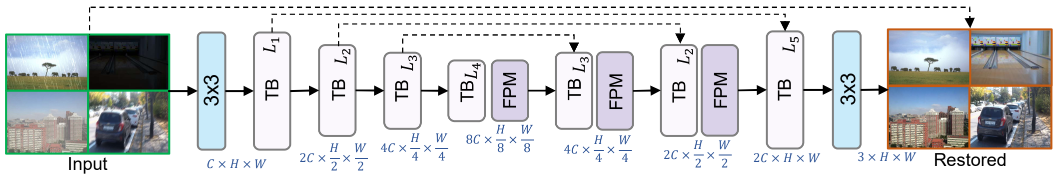

Figure 5: The Transformer model used for all-in-one image restoration. FPM is deployed in the decoder stage following (Potlapalli et al., 2024). The architecture of the Transformer Block (TB) is consistent with (Zamir et al., 2022a).

Table 13: The datasets for three-task and five-task settings. Entries with † are exclusively used for the five-task setting. The noisy images are yielded by adding Gaussian noise of level $\sigma \in \{15, 25, 50\}$.

Task	Denoising	Deraining	Dehazing	Deblurring†	Low-light†
Train	BSD400, WED	Rain100L	RESIDE-β	GoPro	LOL-v1
Test	BSD68,Urban100,Kodak24†	Rain100L	SOTS-Outdoor	GoPro	LOL-v1

Table 14: Comparisons under the three-task setting. A unified model is trained on compound datasets.

	Denoising on BSD68						Deraining on Rain100L		Dehazing on SOTS		Average	
	$\sigma = 15$		$\sigma = 25$		$\sigma = 50$							
Method	PSNR	SSIM	PSNR	SSIM	PSNR	SSIM	PSNR	SSIM	PSNR	SSIM	PSNR	SSIM
BRDNet (Tian et al., 2020)	32.26	0.898	29.76	0.836	26.34	0.693	27.42	0.895	23.23	0.895	27.80	0.843
LPNet (Gao et al., 2019)	26.47	0.778	24.77	0.748	21.26	0.552	24.88	0.784	20.84	0.828	23.64	0.738
FDGAN (Dong et al., 2020b)	30.25	0.910	28.81	0.868	26.43	0.776	29.89	0.933	24.71	0.929	28.02	0.883
MPRNet (Zamir et al., 2021)	33.54	0.927	30.89	0.880	27.56	0.779	33.57	0.954	25.28	0.955	30.17	0.899
DL (Fan et al., 2019)	33.05	0.914	30.41	0.861	26.90	0.740	32.62	0.931	26.92	0.931	29.98	0.876
AirNet (Li et al., 2022)	33.92	0.933	31.26	0.888	28.00	0.797	34.90	0.968	27.94	0.962	31.20	0.910
PromptIR (Potlapalli et al., 2024)	33.98	0.933	31.31	0.888	28.06	0.799	36.37	0.972	30.58	0.974	32.06	0.913
Lin *et al* (Lin et al., 2024)	34.01	0.933	31.39	0.890	28.18	0.802	37.58	0.979	**31.63**	**0.980**	32.56	0.916
Ours	**34.11**	**0.935**	**31.45**	**0.891**	**28.19**	**0.802**	**38.58**	**0.982**	30.85	0.979	**32.64**	**0.918**

Figure 4 shows that frequency prompts effectively recover the corresponding frequency information. For example, the difference in the high-frequency segments is reduced by our high-frequency prompts.

4.2 All-in-One Image Restoration

We further integrate our FPM into a plain Transformer-based backbone (Zamir et al., 2022a) to demonstrate the effectiveness of our method in all-in-one image restoration, which also suggests the adaptability of our FPM to different architectures. Figure 5 showcases the encoder-decoder architecture of the used Transformer block, where FPM is employed only in the decoder stage, following (Potlapalli et al., 2024).

4.2.1 Implementation Details

We evaluate the established model in the three-task setting (Li et al., 2024) (denoising, deraining, dehazing) and five-task setting (Zhang et al., 2023), where motion deblurring and low-light image enhancement are additionally adopted. To train a single model under the three-task or five-task setting, we combine the datasets of those tasks for training (see Table 13). The model is then evaluated using the corresponding test sets of each task. Following (Li et al., 2024), we also experiment under a single-task setting, where the model is individually trained and evaluated for each task.

The all-in-one model is trained using Adam (Kingma & Ba, 2014) with a batch size of 32 for 150 epochs. The learning rate is $2e^{-4}$ and the patch size is $3 \times 128 \times 128$. Random horizontal and vertical flips are adopted for data augmentation. L_1 to L_5 in the model are set to 4, 6, 6, 8, and 8, respectively. Regarding the single-task setting, training setups remain unchanged except for the batch size, which is set to 8.

Table 15: Image deraining comparisons on Rain100L (Yang et al., 2019) for the single-task setting.

Method	UMR	SIRR	MSPFN	LPNet	AirNet	Restormer	PromptIR	**Ours**
PSNR	32.39	32.37	33.50	33.61	34.90	36.74	37.04	**39.03**
SSIM	0.921	0.926	0.948	0.958	0.977	0.978	0.979	**0.985**

Table 16: Image dehazing comparisons in the single-task setting on SOTS-Outdoor (Li et al., 2018).

Method	DehazeNet	AODNet	EPDN	FDGAN	AirNet	Restormer	PromptIR	**Ours**
PSNR	22.46	20.29	22.57	23.15	23.18	30.87	31.31	**31.66**
SSIM	0.851	0.877	0.863	0.921	0.900	0.969	0.973	**0.981**

Table 17: Denoising scores (PSNR/SSIM) for Urban100 (Huang et al., 2015) and BSD68 (Martin et al., 2001) in single-task setting.

	Urban100			BSD68			
Method	$\sigma = 15$	$\sigma = 25$	$\sigma = 50$	$\sigma = 15$	$\sigma = 25$	$\sigma = 50$	Average
CBM3D (Dabov et al., 2007)	33.93/0.941	31.36/0.909	27.93/0.840	33.50/0.922	30.69/0.868	27.36/0.763	30.80/0.874
DnCNN (Zhang et al., 2017a)	32.98/0.931	30.81/0.902	27.59/0.833	33.89/0.930	31.23/0.883	27.92/0.789	30.74/0.878
IRCNN (Zhang et al., 2017b)	27.59/0.833	31.20/0.909	27.70/0.840	33.87/0.929	31.18/0.882	27.88/0.790	29.90/0.864
FFDNet (Zhang et al., 2018a)	33.83/0.942	31.40/0.912	28.05/0.848	33.87/0.929	31.21/0.882	27.96/0.789	31.05/0.884
BRDNet (Tian et al., 2020)	34.42/0.946	31.99/0.919	28.56/0.858	34.10/0.929	31.43/0.885	28.16/0.794	31.44/0.889
AirNet (Li et al., 2022)	34.40/0.949	32.10/0.924	28.88/0.871	34.14/0.936	31.48/0.893	28.23/0.806	31.54/0.897
PromptIR (Potlapalli et al., 2024)	34.77/0.952	32.49/0.929	29.39/0.881	34.34/0.938	31.71/0.897	28.49/0.813	31.87/0.902
Ours	**34.91/0.952**	**32.74/0.931**	**29.72/0.886**	**34.35/0.938**	**31.71/0.897**	**28.50/0.814**	**31.99/0.903**

Table 18: Results (PSNR/SSIM) for the five-task setting. Denoising scores are computed with $\sigma = 25$. The first and second super-lists include the generate and all-in-one restoration methods, respectively.

Method	Dehazing on SOTS	Deraining on Rain100L	Denoising on BSD68	Deblurring on GoPro	Low-Light on LOL	Average
NAFNet (Chen et al., 2022)	25.23/0.939	35.56/0.967	31.02/0.883	26.53/0.808	20.49/0.809	27.76/0.881
HINet (Chen et al., 2021a)	24.74/0.937	35.67/0.969	31.00/0.881	26.12/0.788	19.47/0.800	27.40/0.875
MPRNet (Zamir et al., 2021)	24.27/0.937	**38.16**/0.981	31.35/**0.889**	26.87/0.823	20.84/0.824	28.27/0.890
DGUNet (Mou et al., 2022)	24.78/0.940	36.62/0.971	31.10/0.883	27.25/0.837	21.87/0.823	28.32/0.891
MIRNetV2 (Zamir et al., 2022b)	24.03/0.927	33.89/0.954	30.97/0.881	26.30/0.799	21.52/0.815	27.34/0.875
SwinIR (Liang et al., 2021)	21.50/0.891	30.78/0.923	30.59/0.868	24.52/0.773	17.81/0.723	25.04/0.835
Restormer (Zamir et al., 2022a)	24.09/0.927	34.81/0.962	31.49/0.884	27.22/0.829	20.41/0.806	27.60/0.881
DL (Fan et al., 2019)	20.54/0.826	21.96/0.762	23.09/0.745	19.86/0.672	19.83/0.712	21.05/0.743
Transweather (Valanarasu et al., 2022)	21.32/0.885	29.43/0.905	29.00/0.841	25.12/0.757	21.21/0.792	25.22/0.836
TAPE (Liu et al., 2022)	22.16/0.861	29.67/0.904	30.18/0.855	24.47/0.763	18.97/0.621	25.09/0.801
AirNet (Li et al., 2022)	21.04/0.884	32.98/0.951	30.91/0.882	24.35/0.781	18.18/0.735	25.49/0.846
IDR (Zhang et al., 2023)	25.24/0.943	35.63/0.965	**31.60**/0.887	27.87/0.846	21.34/0.826	28.34/0.893
Ours	**30.90/0.980**	37.99/**0.981**	31.34/0.888	**28.32/0.862**	**23.21/0.846**	**30.35/0.911**

4.2.2 Experimental Results

The quantitative results for the three-task setting are presented in Table 14. Our model performs well on most datasets and metrics. Particularly on the Rain100L (Yang et al., 2019) dataset for image deraining, the performance gain can be as significant as 1 dB PSNR compared to the second-best method (Lin et al., 2024). Moreover, following previous schemes (Li et al., 2022; 2024), we evaluate our model under the single-task setting by training models individually for each task. The results for image deraining, dehazing, and denoising are reported in Table 15, Table 16, and Table 17, respectively. Our model achieves 2.99 dB, 0.35 dB, and 0.12 dB performance gains over the recent state-of-the-art PromptIR (Li et al., 2024) algorithm, which employs spatial prompts. These results demonstrate the superiority of our design.

In addition, we provide the comparisons under the five-task setting in Table 18. Our method is superior to competitors on most tasks. Specifically, our method achieves an average performance

Table 19: Image denoising results (PSNR) on Urban100 (Huang et al., 2015) and Kodak24 (Franzen, 1999). The scores are obtained by directly using the model trained under the five-task setting.

Method	Urban100 $\sigma = 15$	Urban100 $\sigma = 25$	Urban100 $\sigma = 50$	Kodak24 $\sigma = 15$	Kodak24 $\sigma = 25$	Kodak24 $\sigma = 50$	Average
DL (Fan et al., 2019)	21.10	21.28	20.42	22.63	22.66	21.95	21.67
Transweather (Valanarasu et al., 2022)	29.64	27.97	26.08	31.67	29.64	26.74	28.62
TAPE (Liu et al., 2022)	32.19	29.65	25.87	33.24	30.70	27.19	29.81
AirNet (Li et al., 2022)	33.16	30.83	27.45	34.14	31.74	28.59	30.99
IDR (Zhang et al., 2023)	33.82	31.29	28.07	34.78	**32.42**	29.13	31.59
Ours	**34.08**	**31.67**	**28.29**	**34.89**	32.39	**29.22**	**31.76**

Table 20: Ablation studies under the all-in-one setting.

Method	Dehazing on SOTS PSNR	Dehazing on SOTS SSIM	Deraining on Rain100L PSNR	Deraining on Rain100L SSIM	Denoising on BSD68 $\sigma = 15$ PSNR	$\sigma = 15$ SSIM	$\sigma = 25$ PSNR	$\sigma = 25$ SSIM	$\sigma = 50$ PSNR	$\sigma = 50$ SSIM	Average PSNR	Average SSIM
Baseline	28.37	0.956	35.28	0.964	33.82	0.930	31.16	0.884	27.84	0.785	31.29	0.904
PGM	30.17	0.974	36.67	0.973	33.82	0.931	31.16	0.884	27.88	0.788	31.94	0.910
PIM	30.15	0.977	37.13	0.977	33.85	0.931	31.18	0.885	27.91	0.791	32.04	0.912
Full (FPM)	30.97	0.978	37.16	0.978	33.88	0.932	31.21	0.887	27.94	0.792	32.23	0.913

gain of 2.01 dB PSNR over IDR (Zhang et al., 2023). Especially for dehazing on SOTS (Li et al., 2018), the advantage can reach 5.66 dB PSNR. These results indicate the effectiveness of our method. We provide visualizations for all-in-one settings in the Appendix.

Furthermore, we directly apply the model trained under the five-task setting to two out-of-distribution denoising datasets. Table 19 shows that our model has a stronger generalization ability than IDR (Zhang et al., 2023) by producing an average gain of 0.17 dB PSNR. Especially on the Urban100 (Huang et al., 2015) dataset, the advantage can be as large as 0.38 dB PSNR for $\sigma = 25$.

4.2.3 Ablation Studies

We perform ablation studies by training the model for 30 epochs under the three-task setting to demonstrate the effectiveness of our FPM in all-in-one settings. Table 20 shows the Transformer baseline model achieves an average PSNR of 31.29 dB. Our PIM improves performance on all degradation types and levels, resulting in an average gain of 0.75 dB in PSNR. The complete model, incorporating PIM and PGM, further boosts the performance on all datasets, suggesting the efficacy of our design.

5 Conclusion

This paper presents a frequency prompt mechanism (FPM) for image restoration, which is designed by using the implicitly decomposed frequency signals to guide the aggregation of predefined learnable parameters and injecting the learned prompts into the spectra of original input features. More concretely, the prompt generation module leverages the global average pooling to decouple features into different frequency segments for guidance to make prompts encode informative low- and high-frequency information. The obtained prompts are then incorporated with input features via bi-dimensional attention in the spectral domain. FPM can be employed in different architectures. Built on it, the CNN-based network achieves state-of-the-art performance on 15 datasets for five representative image restoration tasks, including image dehazing, defocus deblurring, desnowing, deraining, and low-light image enhancement. Furthermore, equipped with FPM, the Transformer backbone performs favorably against state-of-the-art algorithms in all-in-one restoration settings. These results demonstrate that our design is a valuable contribution to the realm of image restoration.

REFERENCES

Abdullah Abuolaim and Michael S Brown. Defocus deblurring using dual-pixel data. In *Proceedings of the European Conference on Computer Vision*, 2020.

Yuang Ai, Huaibo Huang, Xiaoqiang Zhou, Jiexiang Wang, and Ran He. Multimodal prompt perceiver: Empower adaptiveness, generalizability and fidelity for all-in-one image restoration. *arXiv preprint arXiv:2312.02918*, 2023.

Codruta O Ancuti, Cosmin Ancuti, Mateu Sbert, and Radu Timofte. Dense-haze: A benchmark for image dehazing with dense-haze and haze-free images. In *IEEE International Conference on Image Processing*, 2019.

Liangyu Chen, Xin Lu, Jie Zhang, Xiaojie Chu, and Chengpeng Chen. Hinet: Half instance normalization network for image restoration. In *Proceedings of the IEEE Conference on Computer Vision and Pattern Recognition Workshops*, 2021a.

Liangyu Chen, Xiaojie Chu, Xiangyu Zhang, and Jian Sun. Simple baselines for image restoration. In *Proceedings of the European Conference on Computer Vision*, 2022.

Sixiang Chen, Tian Ye, Yun Liu, Taodong Liao, Jingxia Jiang, Erkang Chen, and Peng Chen. Msp-former: Multi-scale projection transformer for single image desnowing. In *IEEE International Conference on Acoustics, Speech and Signal Processing*, 2023.

Wei-Ting Chen, Hao-Yu Fang, Jian-Jiun Ding, Cheng-Che Tsai, and Sy-Yen Kuo. Jstasr: Joint size and transparency-aware snow removal algorithm based on modified partial convolution and veiling effect removal. In *Proceedings of the European Conference on Computer Vision*, 2020.

Wei-Ting Chen, Hao-Yu Fang, Cheng-Lin Hsieh, Cheng-Che Tsai, I Chen, Jian-Jiun Ding, Sy-Yen Kuo, et al. All snow removed: Single image desnowing algorithm using hierarchical dual-tree complex wavelet representation and contradict channel loss. In *Proceedings of the IEEE International Conference on Computer Vision*, 2021b.

Xiang Chen, Yufeng Li, Longgang Dai, and Caihua Kong. Hybrid high-resolution learning for single remote sensing satellite image dehazing. *IEEE geoscience and remote sensing letters*, 19:1–5, 2021c.

Zixuan Chen, Zewei He, and Zhe-Ming Lu. Dea-net: Single image dehazing based on detail-enhanced convolution and content-guided attention. *IEEE Transactions on Image Processing*, 2024.

Kaichen Chi, Yuan Yuan, and Qi Wang. Trinity-net: Gradient-guided swin transformer-based remote sensing image dehazing and beyond. *IEEE Transactions on Geoscience and Remote Sensing*, 2023.

Sung-Jin Cho, Seo-Won Ji, Jun-Pyo Hong, Seung-Won Jung, and Sung-Jea Ko. Rethinking coarse-to-fine approach in single image deblurring. In *Proceedings of the IEEE International Conference on Computer Vision*, 2021.

Yuning Cui, Wenqi Ren, Xiaochun Cao, and Alois Knoll. Focal network for image restoration. In *Proceedings of the IEEE International Conference on Computer Vision*, pp. 13001–13011, 2023a.

Yuning Cui, Wenqi Ren, Xiaochun Cao, and Alois Knoll. Image restoration via frequency selection. *IEEE Transactions on Pattern Analysis and Machine Intelligence*, 2023b.

Yuning Cui, Yi Tao, Zhenshan Bing, Wenqi Ren, Xinwei Gao, Xiaochun Cao, Kai Huang, and Alois Knoll. Selective frequency network for image restoration. In *International Conference on Learning Representations*, 2023c.

Yuning Cui, Yi Tao, Wenqi Ren, and Alois Knoll. Dual-domain attention for image deblurring. In *Association for the Advancement of Artificial Intelligence*, 2023d.

Kostadin Dabov, Alessandro Foi, Vladimir Katkovnik, and Karen Egiazarian. Color image denoising via sparse 3d collaborative filtering with grouping constraint in luminance-chrominance space. In *IEEE International Conference on Image Processing*, 2007.

Hang Dong, Jinshan Pan, Lei Xiang, Zhe Hu, Xinyi Zhang, Fei Wang, and Ming-Hsuan Yang. Multi-scale boosted dehazing network with dense feature fusion. In *Proceedings of the IEEE Conference on Computer Vision and Pattern Recognition*, 2020a.

Yu Dong, Yihao Liu, He Zhang, Shifeng Chen, and Yu Qiao. Fd-gan: Generative adversarial networks with fusion-discriminator for single image dehazing. In *Proceedings of the AAAI Conference on Artificial Intelligence*, 2020b.

Qingnan Fan, Dongdong Chen, Lu Yuan, Gang Hua, Nenghai Yu, and Baoquan Chen. A general decoupled learning framework for parameterized image operators. *IEEE Transactions on Pattern Analysis and Machine Intelligence*, 2019.

Rich Franzen. Kodak lossless true color image suite. `http://r0k.us/graphics/kodak/`, 1999. Online accessed 24 Oct 2021.

Xueyang Fu, Jiabin Huang, Delu Zeng, Yue Huang, Xinghao Ding, and John Paisley. Removing rain from single images via a deep detail network. In *Proceedings of the IEEE Conference on Computer Vision and Pattern Recognition*, 2017.

Hongyun Gao, Xin Tao, Xiaoyong Shen, and Jiaya Jia. Dynamic scene deblurring with parameter selective sharing and nested skip connections. In *Proceedings of the IEEE Conference on Computer Vision and Pattern Recognition*, 2019.

Hu Gao, Jing Yang, Ning Wang, Jingfan Yang, Ying Zhang, and Depeng Dang. Prompt-based all-in-one image restoration using cnns and transformer. *arXiv preprint arXiv:2309.03063*, 2023.

Chun-Le Guo, Qixin Yan, Saeed Anwar, Runmin Cong, Wenqi Ren, and Chongyi Li. Image dehazing transformer with transmission-aware 3d position embedding. In *Proceedings of the IEEE Conference on Computer Vision and Pattern Recognition*, 2022.

Binghui Huang, Li Zhi, Chao Yang, Fuchun Sun, and Yixu Song. Single satellite optical imagery dehazing using sar image prior based on conditional generative adversarial networks. In *Proceedings of the IEEE Winter Conference on Applications of Computer Vision*, pp. 1806–1813, 2020.

Jia-Bin Huang, Abhishek Singh, and Narendra Ahuja. Single image super-resolution from transformed self-exemplars. In *Proceedings of the IEEE Conference on Computer Vision and Pattern Recognition*, 2015.

Ali Karaali and Claudio Rosito Jung. Edge-based defocus blur estimation with adaptive scale selection. *IEEE Transactions on Image Processing*, 2017.

Diederik P Kingma and Jimmy Ba. Adam: A method for stochastic optimization. *arXiv preprint arXiv:1412.6980*, 2014.

Junyong Lee, Sungkil Lee, Sunghyun Cho, and Seungyong Lee. Deep defocus map estimation using domain adaptation. In *Proceedings of the IEEE Conference on Computer Vision and Pattern Recognition*, 2019.

Junyong Lee, Hyeongseok Son, Jaesung Rim, Sunghyun Cho, and Seungyong Lee. Iterative filter adaptive network for single image defocus deblurring. In *Proceedings of the IEEE Conference on Computer Vision and Pattern Recognition*, 2021.

Bingchen Li, Xin Li, Yiting Lu, Ruoyu Feng, Mengxi Guo, Shijie Zhao, Li Zhang, and Zhibo Chen. Promptcir: Blind compressed image restoration with prompt learning. *arXiv preprint arXiv:2404.17433*, 2024.

Boyi Li, Xiulian Peng, Zhangyang Wang, Jizheng Xu, and Dan Feng. Aod-net: All-in-one dehazing network. In *Proceedings of the IEEE International Conference on Computer Vision*, 2017.

Boyi Li, Wenqi Ren, Dengpan Fu, Dacheng Tao, Dan Feng, Wenjun Zeng, and Zhangyang Wang. Benchmarking single-image dehazing and beyond. *IEEE Transactions on Image Processing*, 2018.

Boyun Li, Xiao Liu, Peng Hu, Zhongqin Wu, Jiancheng Lv, and Xi Peng. All-in-one image restoration for unknown corruption. In *Proceedings of the IEEE Conference on Computer Vision and Pattern Recognition*, 2022.

Ruoteng Li, Robby T. Tan, and Loong-Fah Cheong. All in one bad weather removal using architectural search. In *Proceedings of the IEEE Conference on Computer Vision and Pattern Recognition*, 2020.

Yawei Li, Yuchen Fan, Xiaoyu Xiang, Denis Demandolx, Rakesh Ranjan, Radu Timofte, and Luc Van Gool. Efficient and explicit modelling of image hierarchies for image restoration. In *Proceedings of the IEEE Conference on Computer Vision and Pattern Recognition*, 2023a.

Yu Li, Robby T. Tan, Xiaojie Guo, Jiangbo Lu, and Michael S. Brown. Rain streak removal using layer priors. In *Proceedings of the IEEE Conference on Computer Vision and Pattern Recognition*, 2016.

Yufeng Li and Xiang Chen. A coarse-to-fine two-stage attentive network for haze removal of remote sensing images. *IEEE Geoscience and Remote Sensing Letters*, 18(10):1751–1755, 2020.

Zilong Li, Yiming Lei, Chenglong Ma, Junping Zhang, and Hongming Shan. Prompt-in-prompt learning for universal image restoration. *arXiv preprint arXiv:2312.05038*, 2023b.

Jingyun Liang, Jiezhang Cao, Guolei Sun, Kai Zhang, Luc Van Gool, and Radu Timofte. Swinir: Image restoration using swin transformer. In *Proceedings of the IEEE International Conference on Computer Vision*, 2021.

Jingbo Lin, Zhilu Zhang, Yuxiang Wei, Dongwei Ren, Dongsheng Jiang, Tian Qi, and Wangmeng Zuo. Improving image restoration through removing degradations in textual representations. In *Proceedings of the IEEE Conference on Computer Vision and Pattern Recognition*, 2024.

Lin Liu, Lingxi Xie, Xiaopeng Zhang, Shanxin Yuan, Xiangyu Chen, Wengang Zhou, Houqiang Li, and Qi Tian. Tape: Task-agnostic prior embedding for image restoration. In *European Conference on Computer Vision*, 2022.

Xiaohong Liu, Yongrui Ma, Zhihao Shi, and Jun Chen. Griddehazenet: Attention-based multi-scale network for image dehazing. In *Proceedings of the IEEE International Conference on Computer Vision*, 2019.

Ye Liu, Lei Zhu, Shunda Pei, Huazhu Fu, Jing Qin, Qing Zhang, Liang Wan, and Wei Feng. From synthetic to real: Image dehazing collaborating with unlabeled real data. In *Proceedings of the ACM International Conference on Multimedia*, 2021.

Yun-Fu Liu, Da-Wei Jaw, Shih-Chia Huang, and Jenq-Neng Hwang. Desnownet: Context-aware deep network for snow removal. *IEEE Transactions on Image Processing*, 2018.

Ziwei Luo, Fredrik K Gustafsson, Zheng Zhao, Jens Sjölund, and Thomas B Schön. Controlling vision-language models for universal image restoration. In *International Conference on Learning Representations*, 2021.

Xintian Mao, Yiming Liu, Wei Shen, Qingli Li, and Yan Wang. Deep residual fourier transformation for single image deblurring. *arXiv preprint arXiv:2111.11745*, 2021.

David Martin, Charless Fowlkes, Doron Tal, and Jitendra Malik. A database of human segmented natural images and its application to evaluating segmentation algorithms and measuring ecological statistics. In *Proceedings of the IEEE International Conference on Computer Vision*, 2001.

Chong Mou, Qian Wang, and Jian Zhang. Deep generalized unfolding networks for image restoration. In *Proceedings of the IEEE Conference on Computer Vision and Pattern Recognition*, 2022.

Vaishnav Potlapalli, Syed Waqas Zamir, Salman H Khan, and Fahad Shahbaz Khan. Promptir: Prompting for all-in-one image restoration. *Advances in Neural Information Processing Systems*, 2024.

Xu Qin, Zhilin Wang, Yuanchao Bai, Xiaodong Xie, and Huizhu Jia. Ffa-net: Feature fusion attention network for single image dehazing. In *Proceedings of the AAAI Conference on Artificial Intelligence*, 2020.

Yuwei Qiu, Kaihao Zhang, Chenxi Wang, Wenhan Luo, Hongdong Li, and Zhi Jin. Mb-taylorformer: Multi-branch efficient transformer expanded by taylor formula for image dehazing. In *Proceedings of the IEEE International Conference on Computer Vision*, 2023.

Lingyan Ruan, Bin Chen, Jizhou Li, and Miuling Lam. Learning to deblur using light field generated and real defocus images. In *Proceedings of the IEEE Conference on Computer Vision and Pattern Recognition*, 2022.

Jianping Shi, Li Xu, and Jiaya Jia. Just noticeable defocus blur detection and estimation. In *Proceedings of the IEEE Conference on Computer Vision and Pattern Recognition*, 2015.

Hyeongseok Son, Junyong Lee, Sunghyun Cho, and Seungyong Lee. Single image defocus deblurring using kernel-sharing parallel atrous convolutions. In *Proceedings of the IEEE International Conference on Computer Vision*, 2021.

Yuda Song, Zhuqing He, Hui Qian, and Xin Du. Vision transformers for single image dehazing. *arXiv preprint arXiv:2204.03883*, 2022.

Jingwen Su, Boyan Xu, and Hujun Yin. A survey of deep learning approaches to image restoration. *Neurocomputing*, 2022.

Chunwei Tian, Yong Xu, and Wangmeng Zuo. Image denoising using deep cnn with batch renormalization. *Neural Networks*, 2020.

Fu-Jen Tsai, Yan-Tsung Peng, Yen-Yu Lin, Chung-Chi Tsai, and Chia-Wen Lin. Stripformer: Strip transformer for fast image deblurring. In *Proceedings of the European Conference on Computer Vision*, 2022.

Zhengzhong Tu, Hossein Talebi, Han Zhang, Feng Yang, Peyman Milanfar, Alan Bovik, and Yinxiao Li. Maxim: Multi-axis mlp for image processing. In *Proceedings of the IEEE Conference on Computer Vision and Pattern Recognition*, 2022.

Jeya Maria Jose Valanarasu, Rajeev Yasarla, and Vishal M. Patel. Transweather: Transformer-based restoration of images degraded by adverse weather conditions. In *Proceedings of the IEEE Conference on Computer Vision and Pattern Recognition*, 2022.

Cong Wang, Jinshan Pan, Wei Wang, Jiangxin Dong, Mengzhu Wang, Yakun Ju, Junyang Chen, and Xiao-Ming Wu. Promptrestorer: A prompting image restoration method with degradation perception. In *Thirty-seventh Conference on Neural Information Processing Systems*, 2023.

Cong Wang, Jinshan Pan, Wanyu Lin, Jiangxin Dong, Wei Wang, and Xiao-Ming Wu. Selfpromer: Self-prompt dehazing transformers with depth-consistency. In *Proceedings of the AAAI Conference on Artificial Intelligence*, 2024a.

Tao Wang, Wanglong Lu, Kaihao Zhang, Wenhan Luo, Tae-Kyun Kim, Tong Lu, Hongdong Li, and Ming-Hsuan Yang. Promptrr: Diffusion models as prompt generators for single image reflection removal. *arXiv preprint arXiv:2402.02374*, 2024b.

Zhendong Wang, Xiaodong Cun, Jianmin Bao, Wengang Zhou, Jianzhuang Liu, and Houqiang Li. Uformer: A general u-shaped transformer for image restoration. In *Proceedings of the IEEE Conference on Computer Vision and Pattern Recognition*, 2022.

Haiyan Wu, Yanyun Qu, Shaohui Lin, Jian Zhou, Ruizhi Qiao, Zhizhong Zhang, Yuan Xie, and Lizhuang Ma. Contrastive learning for compact single image dehazing. In *Proceedings of the IEEE Conference on Computer Vision and Pattern Recognition*, 2021.

Wending Yan, Robby T Tan, and Dengxin Dai. Nighttime defogging using high-low frequency decomposition and grayscale-color networks. In *Proceedings of the European Conference on Computer Vision*, 2020.

Hao Yang, Liyuan Pan, Yan Yang, and Wei Liang. Language-driven all-in-one adverse weather removal. *arXiv preprint arXiv:2312.01381*, 2023.

Wenhan Yang, Robby T. Tan, Jiashi Feng, Jiaying Liu, Zongming Guo, and Shuicheng Yan. Deep joint rain detection and removal from a single image. In *Proceedings of the IEEE Conference on Computer Vision and Pattern Recognition*, 2017.

Wenhan Yang, Robby T Tan, Jiashi Feng, Zongming Guo, Shuicheng Yan, and Jiaying Liu. Joint rain detection and removal from a single image with contextualized deep networks. *IEEE Transactions on Pattern Analysis and Machine Intelligence*, 2019.

Wenhan Yang, Wenjing Wang, Haofeng Huang, Shiqi Wang, and Jiaying Liu. Sparse gradient regularized deep retinex network for robust low-light image enhancement. *IEEE Transactions on Image Processing*, 2021.

Tian Ye, Yunchen Zhang, Mingchao Jiang, Liang Chen, Yun Liu, Sixiang Chen, and Erkang Chen. Perceiving and modeling density for image dehazing. In *Proceedings of the European Conference on Computer Vision*, 2022.

Fanghua Yu, Jinjin Gu, Zheyuan Li, Jinfan Hu, Xiangtao Kong, Xintao Wang, Jingwen He, Yu Qiao, and Chao Dong. Scaling up to excellence: Practicing model scaling for photo-realistic image restoration in the wild. In *Proceedings of the IEEE Conference on Computer Vision and Pattern Recognition*, 2024.

Syed Waqas Zamir, Aditya Arora, Salman Khan, Munawar Hayat, Fahad Shahbaz Khan, Ming-Hsuan Yang, and Ling Shao. Multi-stage progressive image restoration. In *Proceedings of the IEEE Conference on Computer Vision and Pattern Recognition*, 2021.

Syed Waqas Zamir, Aditya Arora, Salman Khan, Munawar Hayat, Fahad Shahbaz Khan, and Ming-Hsuan Yang. Restormer: Efficient transformer for high-resolution image restoration. In *Proceedings of the IEEE Conference on Computer Vision and Pattern Recognition*, 2022a.

Syed Waqas Zamir, Aditya Arora, Salman Khan, Munawar Hayat, Fahad Shahbaz Khan, Ming-Hsuan Yang, and Ling Shao. Learning enriched features for fast image restoration and enhancement. *IEEE Transactions on Pattern Analysis and Machine Intelligence*, 2022b.

He Zhang, Vishwanath Sindagi, and Vishal M Patel. Image de-raining using a conditional generative adversarial network. *IEEE transactions on circuits and systems for video technology*, 2019.

Jing Zhang, Yang Cao, Zheng-Jun Zha, and Dacheng Tao. Nighttime dehazing with a synthetic benchmark. In *Proceedings of the ACM International Conference on Multimedia*, 2020.

Jinghao Zhang, Jie Huang, Mingde Yao, Zizheng Yang, Hu Yu, Man Zhou, and Feng Zhao. Ingredient-oriented multi-degradation learning for image restoration. In *Proceedings of the IEEE Conference on Computer Vision and Pattern Recognition*, 2023.

Kai Zhang, Wangmeng Zuo, Yunjin Chen, Deyu Meng, and Lei Zhang. Beyond a gaussian denoiser: Residual learning of deep cnn for image denoising. *IEEE Transactions on Image Processing*, 2017a.

Kai Zhang, Wangmeng Zuo, Shuhang Gu, and Lei Zhang. Learning deep cnn denoiser prior for image restoration. In *Proceedings of the IEEE Conference on Computer Vision and Pattern Recognition*, 2017b.

Kai Zhang, Wangmeng Zuo, and Lei Zhang. Ffdnet: Toward a fast and flexible solution for cnn-based image denoising. *IEEE Transactions on Image Processing*, 2018a.

Kaihao Zhang, Wenqi Ren, Wenhan Luo, Wei-Sheng Lai, Björn Stenger, Ming-Hsuan Yang, and Hongdong Li. Deep image deblurring: A survey. *International Journal of Computer Vision*, 2022.

Yulun Zhang, Kunpeng Li, Kai Li, Lichen Wang, Bineng Zhong, and Yun Fu. Image super-resolution using very deep residual channel attention networks. In *Proceedings of the European Conference on Computer Vision*, 2018b.

Yu Zheng, Jiahui Zhan, Shengfeng He, Junyu Dong, and Yong Du. Curricular contrastive regularization for physics-aware single image dehazing. In *Proceedings of the IEEE Conference on Computer Vision and Pattern Recognition*, pp. 5785–5794, 2023.

Kaiyang Zhou, Jingkang Yang, Chen Change Loy, and Ziwei Liu. Conditional prompt learning for vision-language models. In *Proceedings of the IEEE conference on computer vision and pattern recognition*, 2022a.

Kaiyang Zhou, Jingkang Yang, Chen Change Loy, and Ziwei Liu. Learning to prompt for vision-language models. *International Journal of Computer Vision*, 2022b.

Shihao Zhou, Jinshan Pan, Jinglei Shi, Duosheng Chen, Lishen Qu, and Jufeng Yang. Seeing the unseen: A frequency prompt guided transformer for image restoration. *arXiv preprint arXiv:2404.00288*, 2024.

APPENDIX

This appendix provides specific training configurations for general image restoration, more ablation studies, computational comparisons, and visual comparisons.

A DATASETS AND TRAINING CONFIGURATIONS

In this section, we provide more details of the used datasets and specific training configurations for different general image restoration tasks. According to the complexity of different tasks, we set N to 3 for tasks of dehazing, desnowing, and low-light image enhancement and 15 for deblurring and deraining. Unless specified otherwise, the patch size and batch size adopted for training are $3 \times 256 \times 256$ and 8, respectively. The initial learning rate is set to $2e^{-4}$, which is reduced to $1e^{-6}$ with the cosine annealing strategy.

Image Dehazing. We evaluate our method on four kinds of datasets: synthetic daytime datasets, a real-world dataset, nighttime datasets, and remote sensing datasets. For daytime scenes, we use the widely adopted RESIDE-Indoor (Li et al., 2018) and RESIDE-Outdoor (Li et al., 2018) datasets for training and evaluation. Specifically, the model is trained on these two datasets for 1000 epochs and 30 epochs, respectively, and then tested on the corresponding test sets: SOTS-Indoor (Li et al., 2018) and SOTS-Outdoor (Li et al., 2018). The initial learning rate for RESIDE-Outdoor is set to $1e^{-4}$. Moreover, our method is trained and evaluated on a more realistic synthetic dataset, Haze4K (Liu et al., 2021). The model is trained for 1000 epochs with a batch size of 4 and a learning rate of $1e^{-4}$. Furthermore, our model is trained and tested on the Dense-Haze (Ancuti et al., 2019) datasets to evaluate its robustness in real-world scenarios. The model is trained for 5000 epochs with a batch size of 2 and patch size of 800×1200, following (Cui et al., 2023a; Guo et al., 2022).

In addition to daytime scenes, our model is further evaluated in nighttime scenes. Two commonly used datasets are adopted, *i.e.,* GTA5 (Yan et al., 2020) and NHR (Zhang et al., 2020). Given nighttime hazy images, the ground truth images of these two datasets are nighttime clean images and daytime clean images. The models are trained for 300 epochs on the two datasets with a learning rate of $1e^{-4}$.

Since image dehazing plays an essential role in remote sensing, we evaluate our model on a remote sensing dataset, SateHaze1k (Huang et al., 2020), which consists of three sub-sets with different levels of haze degradations: thin, moderate, and thick. The model is separately trained for three datasets for 1000 epochs with a batch size of 32 and a learning rate of $8e^{-4}$.

Image Defocus Deblurring. Consistent with recent algorithms (Ruan et al., 2022; Cui et al., 2023a; Zamir et al., 2022a), we use the DPDD (Abuolaim & Brown, 2020) datasets for evaluation. This dataset comprises 350, 74, and 76 scenes for training, validation, and testing. There are four images in each scene, named center view, left view, right view, and an all-in-focus ground truth. Our model is trained under the single-image setting by taking the center-view images as input and computing loss values between the output and ground truth. Our training strategy is identical to that of algorithms (Cui et al., 2023a; Ruan et al., 2022).

Image Desnowing. For this task, we use three widely-adopted datasets for training and testing, *i.e.,* CSD (Chen et al., 2021b), SRRS (Chen et al., 2020), and Snow100K (Liu et al., 2018). The preprocessing for these datasets remains identical to previous methods (Chen et al., 2020; Cui et al., 2023a) for fair comparisons. The models are trained for 2000 epochs.

Image Deraining. For image deraining, the model is trained on a compound dataset that is mixed based on (Fu et al., 2017; Yang et al., 2017; Zhang et al., 2019; Li et al., 2016), following (Zamir et al., 2022a; Cui et al., 2023b), and tested on the Test2800 (Fu et al., 2017) dataset. The PSNR/SSIM scores are measured using the Y channel in the YCbCr color space, which is consistent with existing methods (Zamir et al., 2022a; Cui et al., 2023b). The model is trained for 300 epochs with a batch size of 4 and a learning rate of $1e^{-4}$.

Low-Light Image Enhancement. For this task, the model is evaluated on LOL-v2-synthetic (Yang et al., 2021), which consists of 900 and 100 paired images for training and testing, respectively. The model is trained for 2200 epochs on $3 \times 128 \times 128$ patches.

B More Ablation Studies

In this section, more ablation results on general image restoration are provided. We first investigate the influence of the number of prompts in general image restoration. Table 21 shows that the performance improves as we increase the number of paired prompts from 1 to 5. However, more prompts lead to degraded performance, which is probably because of overfitting. As a consequence, we finally chose five paired prompts for better results.

Table 21: Ablation studies for the number of paired prompts.

Number	1	3	5	7	11
PSNR	34.01	35.10	**35.18**	35.03	34.93

Equipped with our mechanism, CNN-based and Transformer-based backbones achieve state-of-the-art performance on two kinds of image restoration tasks. It is necessary to compare our backbone, *i.e.,* without using prompting modules, to previous state-of-the-art algorithms. To this end, we conduct experiments on multiple datasets for different tasks using our baseline models and keep the training configurations identical to the final models. From Table 22 to Table 25, we can see that the baseline model is inferior to previous algorithms. When employing our proposed method, they achieve the state-of-the-art performance, demonstrating the effectiveness of our design.

Table 22: Ablation studies on the SOTS (Li et al., 2018) dataset for image dehazing.

	SOTS-Indoor		SOTS-Outdoor	
Method	PSNR	SSIM	PSNR	SSIM
Baseline	39.07	0.995	34.98	0.993
FocalNet	40.82	0.996	37.71	0.995
DEA-Net	40.20	0.993	36.03	0.989
FSNet-S	40.47	0.996	37.24	0.994
MB-TaylorFormer-B	40.71	0.992	37.42	0.989
Ours	40.86	0.996	37.86	0.995

Table 23: Ablation studies on the Test2800 (Fu et al., 2017) dataset for image deraining.

Method	Baseline	MPRNet	FSNet	**Ours**
PSNR	33.57	33.64	33.64	33.72
SSIM	0.936	0.938	0.936	0.937

Table 24: Ablation studies on SRRS (Chen et al., 2020) and Snow100K (Liu et al., 2018) for image desnowing.

	SRRS		Snow100K	
Method	PSNR	SSIM	PSNR	SSIM
Baseline	30.16	0.98	33.13	0.95
MSP-Former	30.76	0.95	33.43	0.96
FSNet-S	31.39	0.98	33.36	0.95
FocalNet	31.34	0.98	33.53	0.95
Ours	31.78	0.98	33.61	0.95

C Complexity Comparisons

We compare our method with state-of-the-art algorithms on image dehazing and all-in-one image restoration. Figure 6 shows that our model outperforms the recent Transformer-based MB-

Table 25: Ablation studies on the DPDD (Abuolaim & Brown, 2020) dataset for image defocus deblurring.

Method	Indoor Scenes PSNR↑	SSIM↑	MAE↓	LPIPS↓	Outdoor Scenes PSNR	SSIM	MAE	LPIPS	Combined PSNR	SSIM	MAE	LPIPS
Baseline	28.72	0.878	0.025	0.147	23.21	0.750	0.503	0.209	25.89	0.812	0.039	0.178
Restormer	28.87	0.882	0.025	0.145	23.24	0.743	0.050	0.209	25.98	0.811	0.038	0.178
FocalNet	29.10	0.876	0.024	0.173	23.41	0.743	0.049	0.246	26.18	0.808	0.037	0.210
Lin *et al.*	29.11	0.889	-	-	23.35	0.748	-	-	26.15	0.817	-	-
FSNet	29.14	0.878	0.024	0.166	23.45	0.747	0.050	0.246	26.22	0.811	0.037	0.207
Ours	29.38	0.883	0.023	0.145	23.49	0.753	0.049	0.208	26.35	0.816	0.036	0.178

TaylorFormer-B (Qiu et al., 2023) with comparable complexity. Furthermore, as illustrated in Figure 7, our network achieves a significant performance gain over the PromptIR (Li et al., 2024) method in the all-in-one setting, consuming lower complexity. The results demonstrate the efficiency of our design.

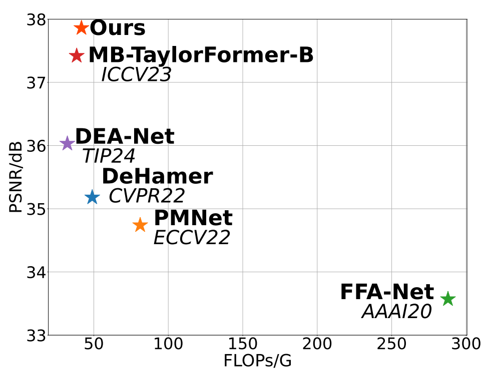

Figure 6: FLOPs *vs.* PSNR on the SOTS-Outdoor (Li et al., 2018) dataset for image dehazing.

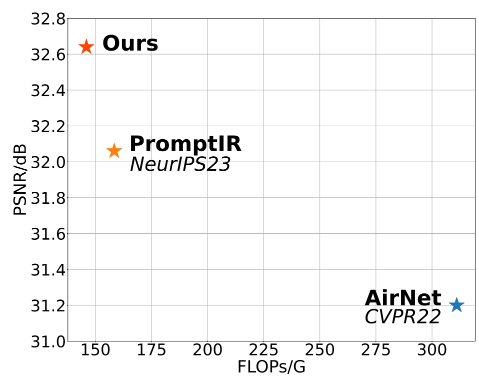

Figure 7: FLOPs *vs.* PSNR for all-in-one models under the three-task setting.

D Visual Comparisons

In this section, we provide visual comparisons for general and all-in-one image restoration tasks.

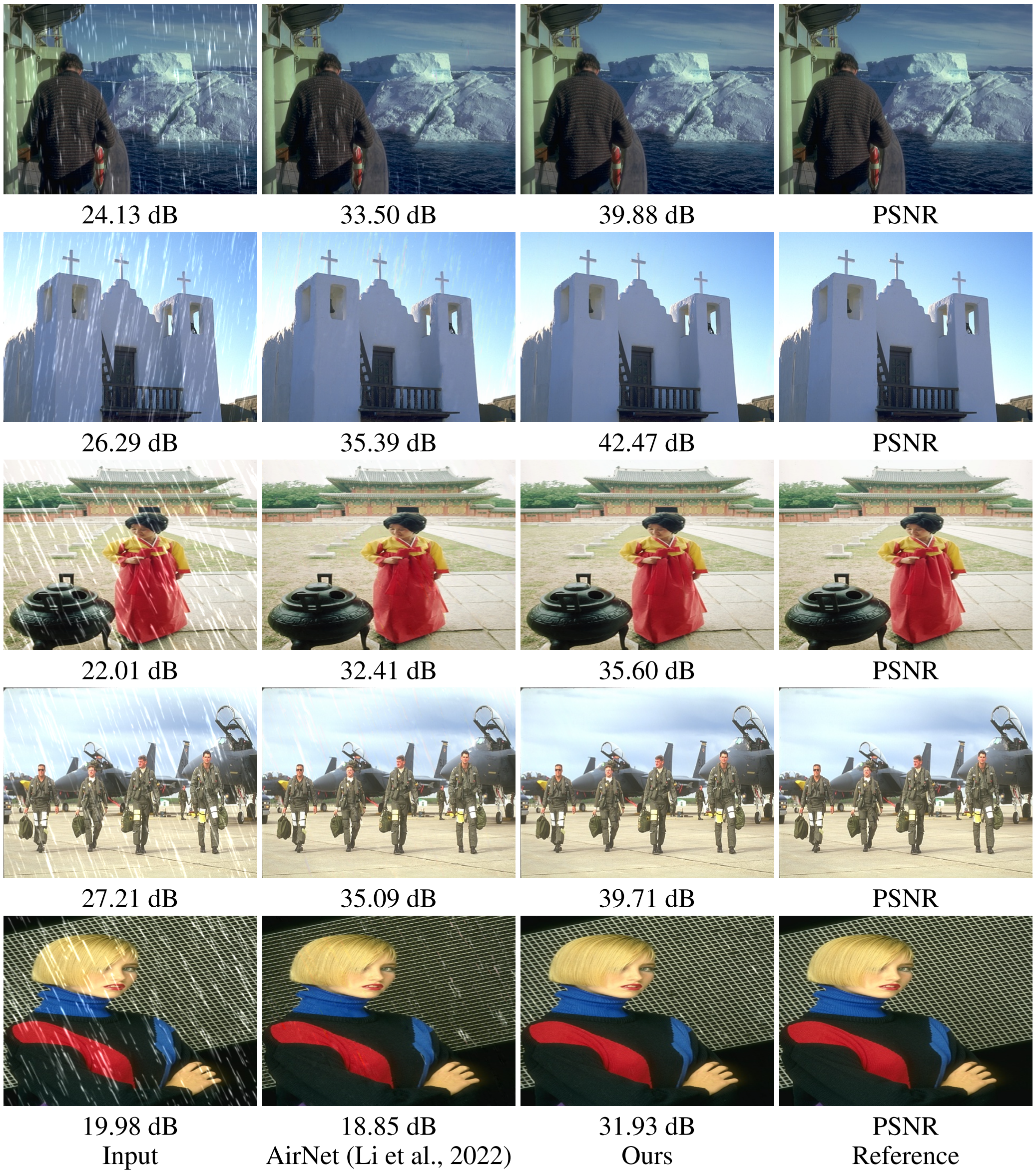

Figure 8: Image deraining comparisons on the Rain100L (Yang et al., 2019) dataset under the single-task setting.

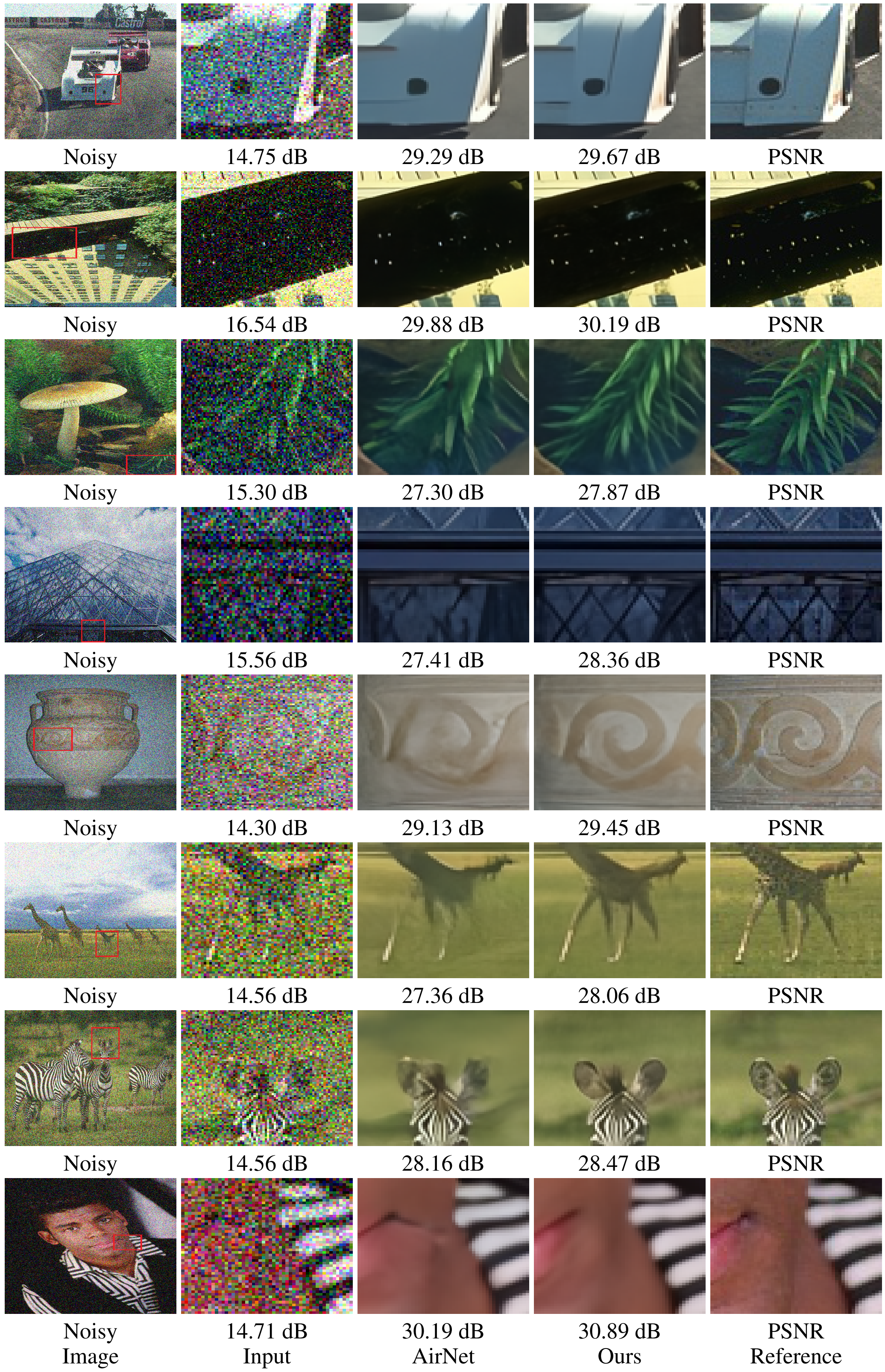

Figure 9: Image denoising comparisons on BSD68 (Martin et al., 2001) with $\sigma = 50$ under the single-task setting.

Figure 10: Image dehazing comparisons on the SOTS-Outdoor (Li et al., 2018) dataset under the single-task setting.

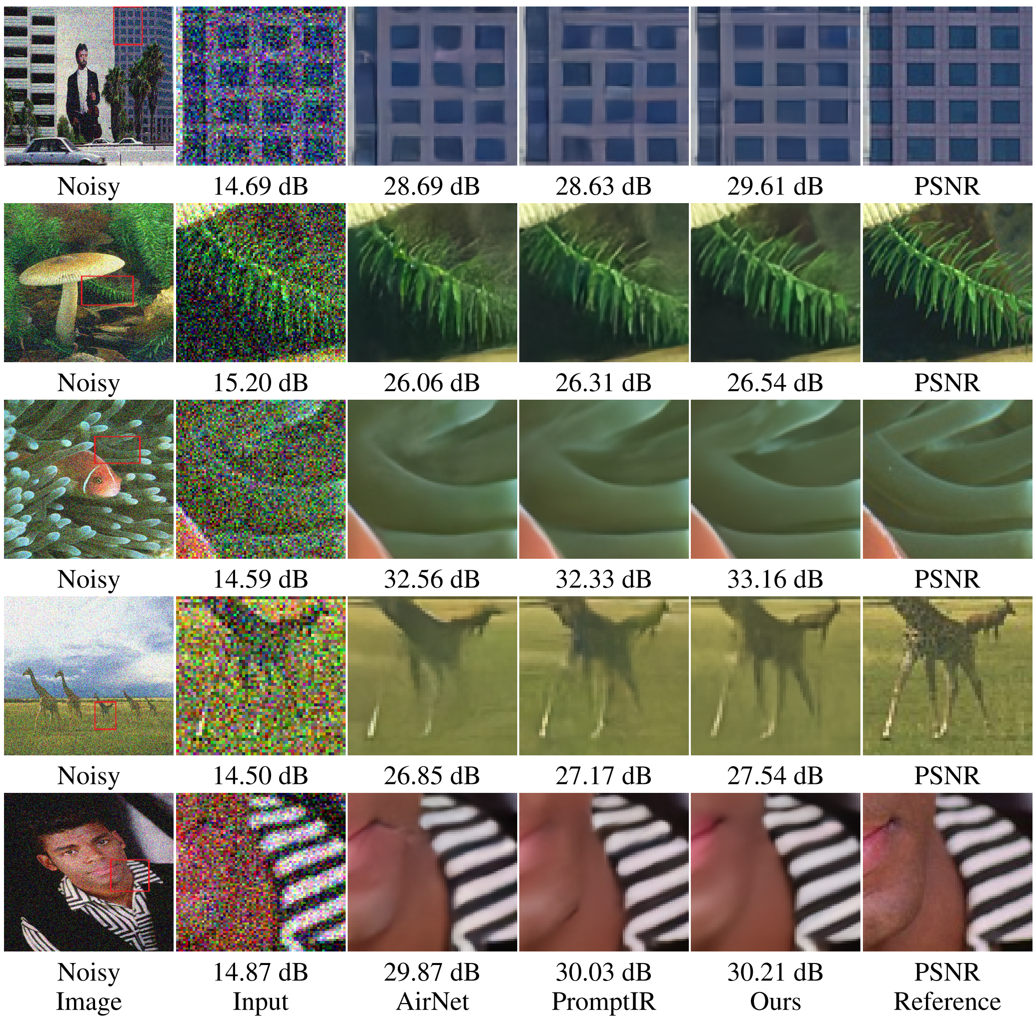

Figure 11: Image denoising comparisons on BSD68 (Martin et al., 2001) with $\sigma = 50$ under the three-task setting.

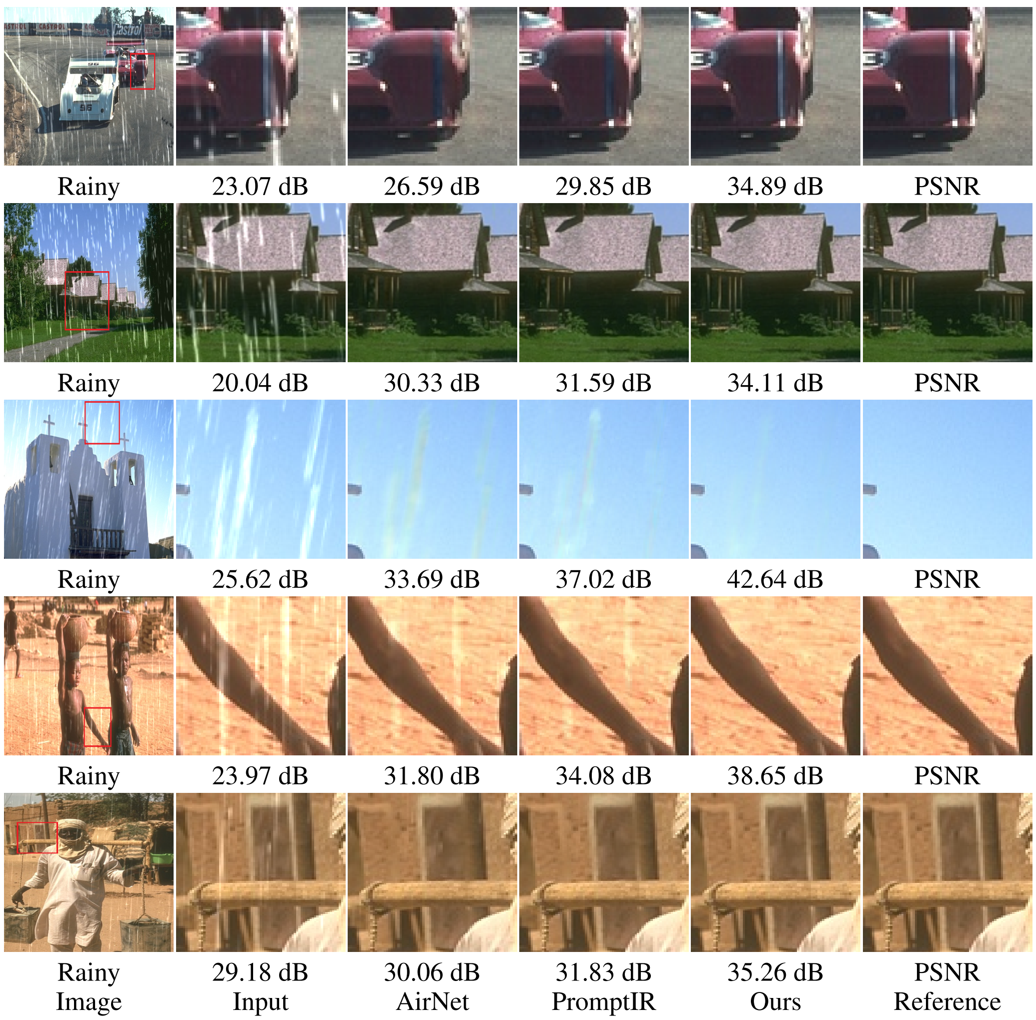

Figure 12: Image deraining comparisons on Rain100L (Yang et al., 2019) under the three-task setting.

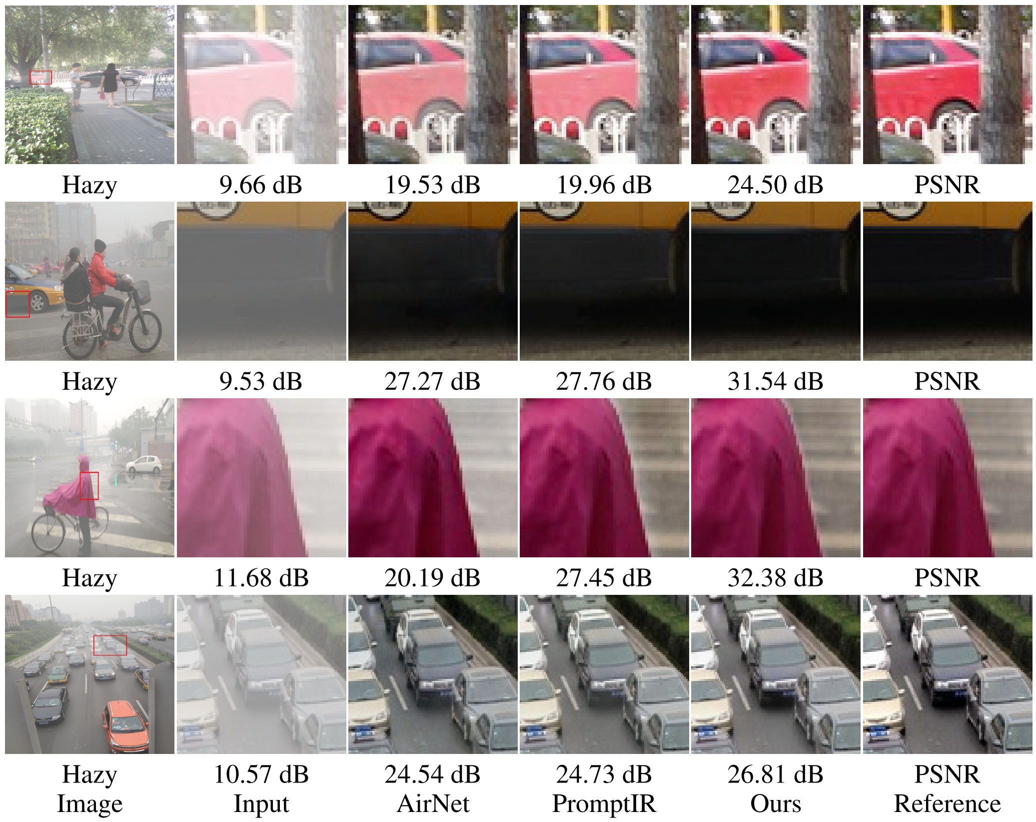

Figure 13: Image dehazing comparisons on SOTS-Outdoor (Li et al., 2018) under the three-task setting.

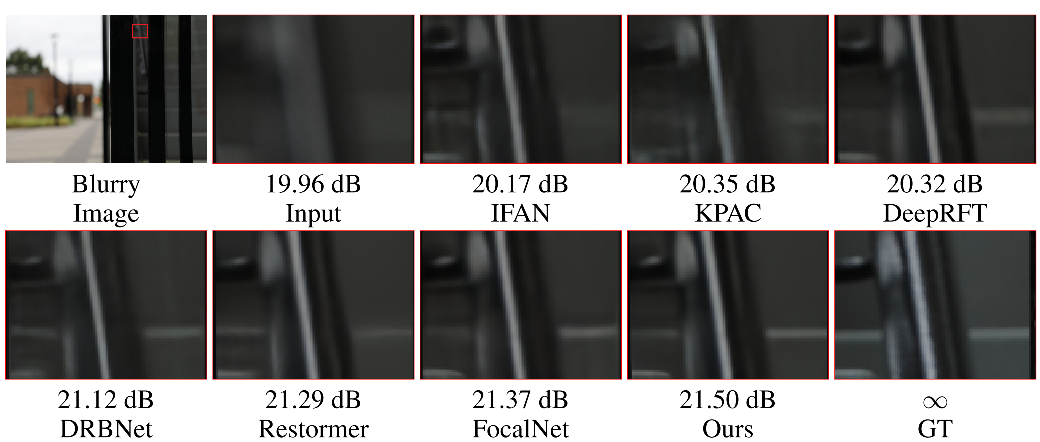

Figure 14: Image defocus deblurring results on the DPDD (Abuolaim & Brown, 2020) dataset.

Figure 15: Image desnowing comparisons on the CSD (Chen et al., 2021b) dataset.

Figure 16: Image dehazing comparisons on the real-world Dense-Haze (Ancuti et al., 2019) dataset.

Figure 17: Image dehazing comparisons on the Haze4K (Liu et al., 2021) dataset.

Figure 18: Low-light image enhancement comparisons on the LOL-v2 (Yang et al., 2021) dataset.

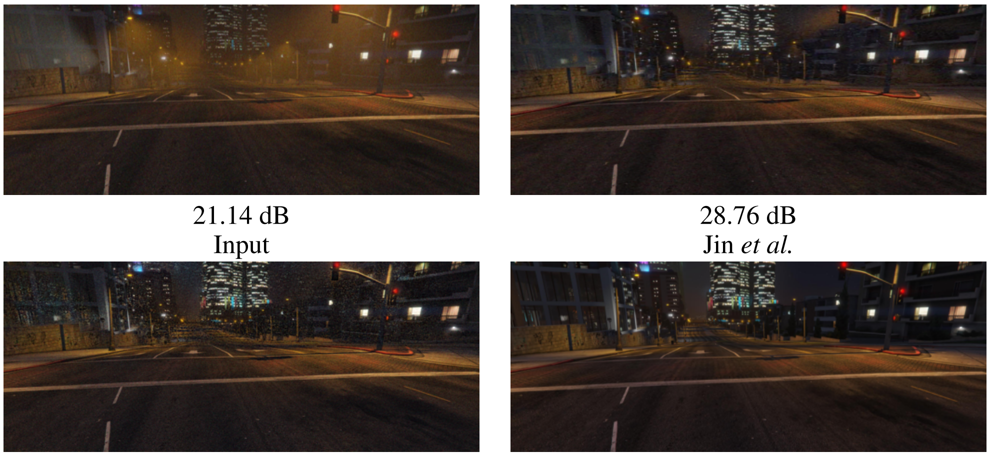

21.14 dB
Input

28.76 dB
Jin *et al.*

30.29 dB
Ours

∞
GT

Figure 19: Image dehazing comparisons on the GTA5 (Yan et al., 2020) dataset.

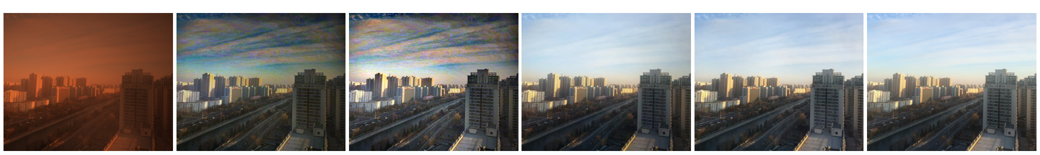

7.52 dB	9.10 dB	11.15 dB	22.88 dB	26.94 dB	∞
Input	OSFD	MRPF	FoalNet	Ours	GT

Figure 20: Image dehazing comparisons on the NHR (Zhang et al., 2020) dataset.